Published in Phys. Rev. B 71, 125316 (2005).

Low-temperature tunneling spectroscopy of Ge(111)c(2 × 8) surfaces

R. M. Feenstra[1] and S. Gaan
Department of Physics, Carnegie Mellon University, Pittsburgh, Pennsylvania 15213
G. Meyer[2]
Paul Drude Institut für Festkörperelektronik, Hausvogteiplatz 5-7, 10117 Berlin, Germany
K. H. Rieder
Institut für Experimentalphysik, Freie Universität Berlin, Arnimallee 14, 14195 Berlin, Germany

Abstract

Scanning tunneling spectroscopy is used to study *p*-type Ge(111)c(2×8) surfaces over the temperature range 7 to 61 K. Surface states arising from adatoms and rest-atoms are observed. With consideration of tip-induced band bending, a surface band gap of 0.5 ± 0.1 eV separating the bulk valence band from the surface adatom band is deduced. Peak positions of adatom states are located at energies of 0.09 ± 0.02 eV and 0.24 ± 0.03 eV above this gap. A spectral feature arising from inversion of the adatom state occupation is also identified. A solution of Poisson's equation for the tip-semiconductor system yields a value for the interband current in agreement with the observations, for an assumed tip radius of 100 nm. The rest-atom spectral peak, observed at ≈ 1.0 eV below the valence band maximum, is observed to shift as a function of tunnel current. It is argued that nonequilibrium occupation of disorder-induced surface states produces this shift.

PACS numbers: 73.20.Hb, 71.20.Nr, 61.16.Ch

I. Introduction

Studies of semiconductors surfaces using scanning tunneling spectroscopy (STS) have been actively pursued for nearly 20 years, but it is only over the past 5 years that measurements at low temperatures have been conducted. The reduction in temperature permits not only a significant increase in spectral resolution but also may allow the study of temperature-dependent transport properties. Recently, interesting temperature-dependent STM and STS results have been reported by Takayanagi and co-workers for for Si(001)2×1 [1], and by Dujardin *et al.* for clean and H-covered Ge(111)c(2×8) [2]. The physical mechanisms behind those results are not completely clear, but it was suggested that temperature-dependent transport of carriers in the semiconductor may in some way be affecting the tunnel current [1-3]. Earlier work at room temperature for SiC(0001)$\sqrt{3}\times\sqrt{3}$-$R30^\circ$ surfaces also demonstrated the existence of transport limitations in the semiconductor during STS experiments [4].

[1] feenstra@cmu.edu
[2] present address: IBM Research Division, Zurich Research Laboratory, 8803 Rüschlikon, Switzerland

In this work we study tunneling spectra acquired from *p*-type Ge(111)c(2×8) surfaces, over the temperature range 7 to 61 K and over a wide range of tunnel currents with setpoint currents (*i.e.* corresponding the current near one of the endpoints of the spectra) ranging from 2 pA to 7 nA. Features arising from the surface adatoms and rest-atoms are identified in the spectra. For large negative sample bias voltages we observe *inversion* of the occupation of the adatom states, thereby conclusively demonstrating the occurrence of tip-induced band bending [5] in the semiconductor. We also observe that the rest-atom peak position shifts markedly as a function of tunnel current. We argue that this effect can be attributed to the tip-induced band bending, but only if we include the influence of defect states associated with c(2×8) domain boundaries. We argue that nonequilibrium occupation (*i.e.* charging) of these states, the amount of which varies with the current, produces the observed rest-atom peak shifts. We observe a temperature dependence of this shift, consistent with that seen by Dujardin *et al.* [2], and this dependence can be accounted for within our model of transport-limited occupation of the defect states.

Detailed electrostatic computations are used to quantify the tip-induced band bending. The two main parameters in the computations are the probe-tip radius of curvature and the density of defect states. For the case of carrier *accumulation* at the surface (positive sample voltage for *p*-type material) the results are relatively independent of the computational parameters and we are able to deduce values of the surface band gap and the energies of the adatom states with considerably greater accuracy than previous measurements [6-8]. For negative voltages, corresponding to semiconductor depletion or inversion, we choose parameter values in the computation to yield agreement with the observed *low-current* values of the inversion voltage and the rest-atom peak position. Then, we find that the *high-current* values for these quantities can be understood by assuming a nonequilibrium occupation of the extrinsic surface states, *i.e.* with a surface Fermi-level that differs from the bulk value. We conclude that transport limitations in the extrinsic states are quite significant at low temperature and high current.

II. Experimental

Low-temperature experiments were performed on *p*-type Ge wafers having resistivity of $0.2\ \Omega$cm , corresponding to a doping concentration of about $2\times10^{16}\ \mathrm{cm}^{-3}$. Pieces of the {111}-oriented wafers were cleaved in ultra-high-vacuum (pressure of about 1×10^{-10} Torr), exposing a (111) crystal face. Cleavage was performed at room temperature, and immediately after cleavage the samples were resistively heated to a temperature of about 500°C for a few minutes. Within a few minutes after heating, the samples were cooled to about 50 K and were introduced into a liquid-He cryostat containing the home-built STM [9]. Probe-tips were formed prior to sample cleavage by making a controlled mechanical contact of a tungsten tip to a clean copper surface, thereby transferring copper atoms to the end of the tip. Metallic tips are reliably formed in this manner [10]. We have obtained spectra from Ge(111)c(2×8) surfaces using several different samples and probe tips, with good overall consistency in the results. The detailed sequence of current- and temperature-dependent spectra described here were,

however, obtained using a single probe tip, with no large tip changes either performed or observed during the measurements.

We have also performed experiments at room temperature, using an STM previously described [11]. In this case *n*-type Ge with resistivity of $0.2\ \Omega$cm was studied. Samples were cleaved and annealed in an identical manner as for the low-temperature work. Pt-Ir probe tips were used, cleaned by electron bombardment [11]. Spectra were acquired both simultaneous with images and at times between image acquisition. With a drift-rate in the STM of less then 0.2 nm/min, and having images acquired at known times separated by 5-10 minutes, the spatial locations of all spectra are known to an accuracy of better than 0.5 nm.

Tunneling spectra were acquired using a voltage modulation of 10–20 mV and employing a lock-in amplifier to obtain the conductance. The technique of continuously varying sample-tip separation was used to obtain a large dynamic range in the measurements [12], applying an offset to the sample-tip separation of the form $\Delta s(V) = a|V|$ where V is the sample-tip voltage. Values of a are chosen to obtain conveniently measurable current and conductance values, with a value of about 1 Å/V typically being used (separate values of a are used for positive and negative voltages).

Normalization of the spectra was done in two steps. First, we scale the results to constant sample-tip separation using the scaling factor $\exp(2k\,\Delta s)$ where values of k are determined experimentally [11]. We find k values to be generally within $\pm 0.1\ \text{Å}^{-1}$ of the value $1.0\ \text{Å}^{-1}$, except for large negative voltages where they fall to as low as $0.5\ \text{Å}^{-1}$. In this latter case we believe that the reduced values arise from tip-induced band bending, which is most predominant at these voltage as discussed Section IV. We note that changes in the calibration of the STM piezoelectric elements were carefully included in our analysis; these changes were determined by observations of unit cell dimensions and step heights at the various temperatures. Results for the conductance at constant sample-tip separation are displayed below, using a logarithmic scale to reveal the 3-4 orders of magnitude range in the data. The second step in the normalization, done to permit viewing of the data on a linear scale, is to compute the ratio of differential conductance to total conductance, $(dI/dV)/\overline{(I/V)}$. The denominator of this quantity is formed by applying some broadening to (I/V) in order to form a suitable normalization quantity (*i.e.* to avoid divergences which otherwise occur at the band edges [11,12]). $\overline{(I/V)}$ is formed according to Eq. (5) of Ref. [11], using parameter values of $a' = 2\ \text{V}^{-1}$ and $\Delta V = 1\ \text{V}$ as defined there.

III. Results

A. Surface structure

The structure of the Ge(111)c(2×8) surface is well established. It consists of an arrangement of adatoms and rest-atoms on the surface, with each c(2×8) unit cell

consisting of a sequence of 2×2 and c(2×4) local geometries [6]. Surface states are associated with rest-atoms and adatoms, with the former states being completely filled with electrons and the latter empty. There are two inequivalent sites for both adatoms and rest-atoms in each c(2×8) cell, leading to a small energetic splitting within each surface band [13,14]. An STM image of the surface obtained using our preparation method is shown in Fig. 1. We find well-ordered c(2×8) domains with diameter of about 50 nm, separated by domain boundaries in which the adatom and rest-atom arrangement is somewhat disordered. This arrangement of ordered domains is well understood on the basis of how the c(2×8) structures forms during annealing of the cleaved surface [8].

As will be discussed in Section IV, an important parameter that is needed to fully understand our observed tunneling spectra is the density of *extrinsic* surface states arising from defects and disorder on the surface (these states produce surface charging, which leads to observed spectral shifts). We can roughly estimate the density of such states based on STM images such as Fig. 1. We observe a typical diameter of ordered domains of about 50 nm, and they are surrounded by domain boundaries about 2 nm wide. If we assume 2 dangling bond states (one adatom and one rest-atom) for each 2×2 unit cell of the boundary, we arrive at a total density of extrinsic surface states of about 3×10^{13} cm^{-2}, or 0.04 monolayers.

B. Tunneling spectra

Low-temperature tunneling spectra were acquired over well-ordered c(2×8) regions, and the spectra displayed here consist of spatially averaged results composed generally of 10-20 individual spectra acquired at various points through the c(2×8) unit cell. (Detailed spatially-resolved spectra were also examined during the course of the study, and they display results as expected with the adatom and rest-atom derived peaks being localized at their respective spatial locations). In Fig. 2 we display results for a spectrum acquired at a temperatures of 61 K, and for a tunnel current setpoint of 7 pA. The tunnel current setpoint is defined as the constant-current used for STM imaging prior to acquisition of the spectra; the voltage used for that imaging corresponds to a voltage near one of the endpoints of each spectra (approximately +2.0 or -2.0 V). The current setpoint thus determines the sample-tip separation, with this separation decreasing by about 1.0 Å for each order-of-magnitude increase in current setpoint.

A number of features can be readily identified in the spectrum of Fig. 2. A band gap is visible extending from about -0.1 to 0.5 V. The surface Fermi-level (0 V in the spectrum) is located near the bottom of the gap, as expected for *p*-type material. A large spectral peak is seen centered at about 0.7 V and it can be attributed to the empty states associated with the surface adatoms [6,8], in agreement with inverse photoemission results [7]. This spectral peak appears to have two components, consistent with the expectation of a splitting due to the two inequivalent types of adatoms in the c(2×8) structure [13] (theoretically, this splitting is expected to be 0.2 eV [14]). In the filled states, at about -1.0 V, a spectral feature deriving from the surface rest-atoms is visible. This rest-atom band is resonant with valence band (VB) states [15], with the VB

maximum seen in the spectra at about -0.1 V. As discussed below the location of the rest-atom peak shows a continuous variation as a function of current, but the low-current position of -0.9 eV relative to the VB maximum is in reasonable agreement with the location seen in photoemission of -0.7 eV [15]. Finally, above the adatom band, at voltages above +1.0 V, the current derives either from conduction band (CB) states or possibly from higher-lying surface bands. The observed surface gap is thus seen to be bounded by bulk VB states at its lower edge and surface adatom-derived states at its upper edge.

To investigate the effect of surface disorder on the distribution of surface states we have acquired spatially-resolved spectra near domain boundaries of the c(2×8) structure. These studies were performed at room temperature, with results shown in Fig. 3 for spectra acquired at well-ordered and disordered locations. The specific spatial locations for the spectra of Fig. 3(b) are shown in the image of Fig. 3(a). (The spatial areas for the spectra of Fig. 3(c) are not shown, but they are similarly far and near, respectively, from a domain boundary). The spectra from ordered areas display a band gap, extending from $+0.1$ down to -0.4 or -0.5 V, with adatom and rest-atom states visible on either side of this gap. The spectra of Figs. 3(b) and (c) were acquired with different probe-tips and display somewhat different spectral magnitudes, an effect we tentatively attribute to differences between the electronic structure of the respective tips. Nevertheless, the difference between ordered and disordered results can be clearly seen for each probe-tip. In Fig. 3(b), the spectrum acquired near the defect on the domain boundary displays an additional peak centered at about -0.5 V and extending well into the lower part of the band gap. For Fig. 3(c), the disordered spectrum displays significant narrowing of the gap, *i.e.* tailing of the band states into the band gap.

C. Curve fitting of spectral features

Curve fitting of selected portions of the spectra has been performed in order to derive values for onsets and peak positions. For tunneling into the bulk effective-mass bands it has been previously found that a linear onset for the conductance *vs.* voltage provides a good fit to the data [11]. This linear behavior is also expected on the basis of a WKB analysis of tunneling behavior for a planar junction [16]. We employ here a generalization of the linear form that includes broadening effects due to both temperature and the modulation voltage of the lock-in amplifier used for the measurement. Assuming that the band onset eV_0 is well separated from the sample Fermi-level, the resulting form for the conductance (or normalized conductance) is found to be [17]

$$g_1(V) = a\left[(V - V_0) + b\,\ln\left(1 + e^{-(V-V_0)/b}\right)\right] \tag{1}$$

where V is the sample voltage, a is an amplitude parameter, and b is a voltage interval given by

$$b = \left[(kT/e)^2 + (0.4\,V_{rms})^2\right]^{1/2} \tag{2}$$

where T is the temperature and V_{rms} is the *rms* modulation voltage. The second term on the right-hand side of Eq. (2) provides an approximate means of including the effects of the modulation voltage. The value of 0.4 appearing there is chosen such that fits of this form to simulated conductance characteristics (computed from the WKB formula for planar tunneling) faithfully produce accurate results for the band onsets [17]. Equation (1) is suitable for a band that extends over $E > eV_0$; the appropriate form for one that extends over $E < eV_0$ can be obtained by replacing both occurrences of $(V - V_0)$ in the equation by $(V_0 - V)$. Using this functional form we perform fits to the VB onset of our spectra, with Fig. 4(a) showing the result for the spectrum of Fig. 2. The linear behavior of the onset is found to fit the data quite well. Regarding the onset of the adatom band, this behavior will in general depend on the dispersion of that surface state band. Nevertheless we find that a linear onset also fits this data reasonably well and we therefore utilize it. The resulting fit is shown in Fig. 4(b).

For the rest-atom band the data indicates a relatively broad feature, as might be expected since this band is resonant (*i.e.* degenerate in energy) with VB states. The peak positions can be determined directly from the data without the need for curve fitting. For the adatom band, that spectral feature actually contains two separate bands, which we separate by curve fitting. The lowest-energy adatom band extends into the bulk band gap, and as mentioned above a linear function provides a good description of its onset. Therefore, to describe the lowest-energy adatom band we use a function of the form

$$g_2(V) = b(V - V_1)\exp\left\{-(V - V_1)^2 / \left(2dV^2\right)\right\} \qquad (3)$$

where b, V_1, and dV are parameters. This function has a maximum at a voltage of $V_1 + dV$. For the higher-energy adatom band we use a Gaussian function. The resulting fit is shown in Fig. 4(c) where we see that a reasonable description of the two overlapping bands is obtained. The low-energy onset is *not* precisely described by this fit since we have not included broadening of the onset due to temperature and modulation voltage in Eq. (3), but this inaccuracy has little impact on the rest of the fit and in any case we fit the onset region separately as described in the previous paragraph.

Curve fitting has been performed on a series of spectra acquired at temperatures of 7, 15, and 61 K and with setpoints currents ranging from 2 pA - 7 nA. A number of these spectra have been displayed in our previous work [18]. A summary of the results for the VB onset and adatom features is given in Fig. 5, where we plot the voltage of each spectral feature as a function of the sample-tip separation corresponding to those voltages. The latter is obtained from knowledge of the set-point current for each spectrum, assuming a change in separation with setpoint current in accordance to the k value of 1.0 Å^{-1}, and using the known $\Delta s(V)$ characteristics for each spectra. The zero in sample-tip separation is not precisely known, but as discussed in our prior work [18] we assume a separation of 7 Å for a setpoint current of 1 nA (at sample voltage of +2 V), and we can be quite confident that the actual separation values are not *less* than those given in Fig. 5 and they might be 1 - 2 Å greater. For the VB onset, adatom band onset, and the adatom peak positions, we find results that are relatively independent of

temperature and current. Resulting values are -0.111 ± 0.039 V, 0.495 ± 0.012 V, 0.594 ± 0.012 V, and 0.760 ± 0.018 V, respectively, where the uncertainties indicate the standard deviation of the measured values in each case.

In contrast to the observed results for the VB maximum and the adatom spectral features, the position of the rest-atom peak displays a large variation with current setpoint and temperature, as shown in Fig. 6. We plot in this case the peak position as a function of the *actual* current (not the setpoints) measured in each case. For convenience we can *approximately* convert this current scale into a scale of sample-tip separation, as shown at the top of Fig. 6. This conversion is not exact since we are discussing spectral feature at different voltages, but over the voltage range of interest this separation scale is correct for relative separations to within ± 0.2 Å. Also, the same uncertainty in the zero of this separation scale occurs as described above for Fig. 5.

D. Semiconductor inversion

In addition to the spectral features discussed above we observe one additional voltage-dependent feature in our experiments. In Fig. 7(a) - (f) we present six constant-current STM images, selected from a series of 15 images acquired at closely-spaced sample voltages ranging from -2.5 to $+2.1$ V. For Ge(111)c(2×8) surfaces it is well known that at negative sample voltages (filled states) the surface rest-atoms are imaged and at positive sample voltages (empty states) the surface adatoms are imaged [6,8]. This behavior is clearly seen in Fig. 7 comparing the positive-voltage image at $+1.7$ V with the negative-voltage ones for voltages between -1.8 and -2.0 V. However, at negative voltages below about -2.0 V we observed a remarkable transition in which the *adatoms* again become dominant in the images, as seen by the close similarity between Figs. 7(a) and (f). This behavior persists for negative voltages with larger magnitude. This transition in the STM images is also apparent in the tunneling current vs. voltage characteristics themselves - we consistently observe a sharp discontinuity in the tunnel current at voltages near -2 V, just when the contrast of the images changes from rest-atoms to adatoms, as shown in Fig. 7(g).

We interpret the observed transition in the voltage-dependent images near -2 V to be due to *inversion* of the occupation of surface electronic states. The adatom-derived states are, of course, normally empty. However at a sufficiently large negative sample-tip voltage tip-induced band bending can cause these empty states to occur at an energy below the sample Fermi-level and in that case the adatom states may become occupied, as long as the supply rate of electrons into these states from the semiconductor is sufficiently large. In Section IV(C) we perform detailed computations of the interband current, and we indeed find values that are comparable to the tunnel currents used in our experiments.

IV. Discussion
A. Tip-induced band bending

It is well known that during STS experiments on semiconductor surfaces the applied potential between sample and tip will extend into the semiconductor [5], a phenomena which is generally referred to as *tip-induced band bending*. This effect occurs predominantly when the semiconductor is in depletion, *i.e.* negative sample voltage for *p*-type material and positive sample voltage for *n*-type material. Let us denote the electrostatic potential in the semiconductor by $V(r,z)$, where we are using cylindrical coordinates (r,z) with the semiconductor spanning the half-space $z<0$. Charge densities in the semiconductor are computed in a semi-classical approximation by assuming that the energy bands at a particular location are simply shifted in energy by the electrostatic potential energy, $f(r,z)=-eV(r,z)$ with the zero of $V(r,z)$ taken to be at a point far inside the semiconductor ($z\to-\infty$). Thus, if the charge density with $f=0$ is given by $r(E_F)$ where E_F is the Fermi-level, then the charge density in the presence of a nonzero electrostatic potential is given by $r(E_F-f(r,z))$. Poisson's equation then becomes

$$\nabla^2 f(r,z)=\frac{e\,r(E_F-f(r,z))}{e\,e_0} \tag{4}$$

where e_0 is the permittivity of vacuum and e is the dielectric constant of the semiconductor. Recently, a finite-element method for solving this equation for a 3-dimensional hyperbolic tip geometry was presented by one of us [19]. The computations presented below are based on that computational method together with a few extensions as described in Appendix I, the most important of which is the inclusion of surface states. We assume that the occupation of surface states can be described in terms of a surface Fermi-level, $E_{F,S}$, which in general may be different than the bulk Fermi-level. Denoting the surface charge density with $f=0$ as $s(E_{F,S})$, the boundary condition at the surface is given by

$$\frac{\partial f}{\partial z}(r,0_+)=e\,\frac{\partial f}{\partial z}(r,0_-)+\frac{e\,s(E_{F,S}-f(r,0))}{e_0}\ . \tag{5}$$

When equilibrium exists between the bulk and surface states we have $E_{F,S}=E_F$.

Far inside the semiconductor the electrostatic potential energy is taken to be constant, with a value of zero (use of a variable-spacing grid, described in Appendix I, enables a sufficiently large simulation region inside the semiconductor even for low or zero semiconductor doping). The boundary condition at the probe-tip surface is that the potential energy there equals a specified value, f_T. This theoretical parameter is related to the experimentally specified sample-tip voltage, V_S, by [19]

$$f_T=eV_S+\Delta f \tag{6a}$$

where the *contact potential* is given by

$$\Delta f \equiv f_m - c - \left(E_{C,S}^{\infty} - E_F\right) \tag{6b}$$

where f_m is the work function of the metallic tip and c is the electron affinity of the semiconductor. The quantity $\left(E_{C,S}^{\infty} - E_F\right)$ is the difference in energy between the CB minimum at the surface and the Fermi-level, for a situation where the probe-tip is located infinitely far from the semiconductor.

Surface charge density can arise from *intrinsic* (*i.e.* associated with an ordered surface reconstruction) or *extrinsic* (derived from defects and/or disorder) states on the surface. The question of what type of distribution of midgap states arises from surface defects or disorder is one which has been considered for various semiconductor surfaces [20]. A variety of models have been introduced ranging from exponential tails of states extending in from the band edges to a Gaussian distribution of states located near the middle of the band gap. The major type of disorder on our surfaces are the boundaries which separate the c(2×8) domains, as seen in Fig. 1. The disordered arrangement of adatoms and rest-atoms seen there is expected to produce dangling bond states spread throughout the energy region separating the rest-atom and adatom bands of the c(2×8) structure, and indeed we directly observe such states in the room-temperature STS results of Fig. 3.

The precise distribution of midgap states is not crucial to the arguments below, and we adopt a model consisting simply of a uniform distribution of states, as pictured in Fig. 8. To assign the charge of the states we use the well-known concept of a *charge neutrality level*, E_N, above which the states have acceptor character (negative when occupied and neutral when empty) and below which the states have donor character (neutral when occupied and positive when empty) [20]. We place the charge neutrality level at an energy approximately midway between the intrinsic bands, at 0.2 eV above the VB maximum, E_V. Our assumed surface charge density due to extrinsic states is thus

$$s(E) = \begin{cases} -\left(E_A - E_N\right)s' & E > E_A \\ -\left(E - E_N\right)s' & E_V < E < E_A \\ -\left(E_V - E_N\right)s' & E < E_V \end{cases} \tag{7}$$

where $s' > 0$ is a constant. In this equation we have truncated the extrinsic state density at energies of E_V and E_A, where the latter is the minimum energy of the intrinsic adatom band which according to the results of Section IV(B) is located at $E_V + 0.5$ eV. This truncation is performed because defect states outside this range are degenerate with continuum states and therefore incapable of holding charge. Concerning a value for s', we estimated in Section III(A) a total density of extrinsic states of about 3×10^{13} cm^{-2}. Most of these states would have energies within or close to the adatom or rest-atom bands, with a lesser number lying in the energy region between the bands. Taking one-tenth of the states to lie in the ≈ 1 eV energy gap between the adatom and rest-atom bands, we arrive at an order-of-magnitude estimate for s' of 3×10^{12} cm^{-2}eV^{-1}.

Our model of extrinsic states is a spatially uniform one, even though in reality these states are localized mainly near the c(2×8) domain boundaries. Charge contained in the midgap extrinsic states is balanced by the space charge in the depletion region of the semiconductor, with a depletion width of 100 nm for the doping concentration of our samples and a typical band bending of 0.1 eV. This value is larger than the typical extent of domains on the surface, 50 nm, so that the band bending induced by the extrinsic states will be relatively uniform over a domain. Our treatment of the extrinsic state density as spatially uniform is thus reasonably well justified.

Figure 9 shows computational results for the surface band bending at the surface location on the central axis, $f_0 \equiv f(0,0)$, for various values of the sample voltage and as a function of the extrinsic surface charge density s', and assuming equilibrium between bulk and surface states. The computations are performed for the known doping concentration of our *p*-type Ge samples, 2×10^{16} cm^{-3}, and for a temperature of 0 K (increasing the temperature to, say, 60 K has only a very small effect on the results primarily through a shift in the sample Fermi-level position of about 15 meV). We assume in Fig. 9 a probe tip radius of curvature of 100 nm. For the bulk charge density we use a single effective mass band, *i.e.* the Ge valence band, using a valence band density-of-states effective mass [21] of $m_{dh} = \left[\left(m_{lh}^{*} \right)^{3/2} + \left(m_{hh}^{*} \right)^{3/2} \right]^{2/3} = 0.35\, m_0$ where m_{lh}^{*} and m_{hh}^{*} are the light and heavy-hole masses, respectively, with values of $0.043\, m_0$ and $0.34\, m_0$ for Ge [22]. We see from Fig. 9 that the effect of the extrinsic surface states is to reduce the tip-induced band bending. The surface states charge up in accordance to the sign of the sample-tip voltage and in this way the boundary condition, Eq. (5), can be satisfied using a smaller electric field in the semiconductor. For large values of s' the surface potential energy approaches a position equal to that of the assumed charge neutrality level of the surface state distribution.

In addition to the surface defect state density, the other main parameter in determining the tip-induced band bending is the tip radius-of-curvature. Tip radius is especially important for situation such as the present case with moderate or low doping, since in a 1-D computation nearly all of the applied sample-tip voltage is dropped in the semiconductor but in 3-D this band bending decreases significantly even for rather blunt tips. In the following sections we present computational results as a function of tip radius. The opening angle of the tip shank can also be varied on our computations [19], but we keep this fixed at 90° for all the results described here. Other computational parameters are the contact potential, already discussed above, and the sample-tip separation. The latter does change slightly in our experiments, in accordance with the current set-point, but as discussed in our prior work [18] this variation is far too small to account for our observed shift in the rest-atom peak as a function of current. Some uncertainty in the zero of sample-tip separation exists but this uncertainty has relatively little effect on our comparison between experiment and theory described below.

B. Surface band gap

The position of the Ge(111)c(2×8) rest-atom band is fairly well known, lying at a central location of $E_V - 0.7$ eV as discussed in Section III(C). However, the position of the adatom band is *not* well known and, in particular, no previous value for the surface band gap (difference between adatom band onset and VB maximum) has been reported. In this section we derive an approximate value for the surface gap, taking into account the possibility of tip-induced band bending but without assuming any particular values for the parameters involved in this band bending.

As discussed in Section III(C) we observe the onset of the adatom band to be at 0.495 ± 0.012 V and the onset of the VB to be at -0.111 ± 0.039 V. The difference between these values leads to a upper bound for the surface gap of about 0.60 eV. Tip-induced band bending will act to reduce this estimated gap value. A worst-case situation is when no surface states exist and the tip radius is very large. Actually, from our computational results we find that in the accumulation regime the variation in band bending with tip radius is very small (less than 0.01 eV) for radii above 10 nm, so we can use the results shown in Fig. 9 to estimate the band bending. Considering a sample voltage of $+0.5$ V and zero surface charge density we find a band bending of $+0.10$ eV. Thus, a band edge at 0.4 eV would be observed at a sample voltage of 0.5 V, neglecting any possible contact potential between tip and sample (see discussion surrounding Eq. (6)). Allowing for a positive contact potential would mean that a band edge at 0.4 eV would be observed at a slightly *lower* sample voltage, or in other words, the observed band edge at 0.5 V would correspond to a band gap slightly *larger* than 0.4 eV. A negative value for the contact potential can be ruled out, for the present assumption of zero surface states, since the observed position of the VB onset is significantly below 0 V. We thus deduce a lower bound for the surface band gap of 0.40 eV.

Using our estimated upper and lower bounds for the surface band gap, we assign a value of 0.5 ± 0.1 eV to this gap, where the error estimate is a conservative one. We note at this point that the results of Fig. 9 are *semi-classical*, and localized states in the accumulation layer may in principle produce different band bending. However we have also made a self-consistent quantum mechanical computation of the accumulation layer charge density, as described in Appendix II, and we find that for the cases of relevance here that the semi-classical approximation produces results that are accurate to within 0.02 eV. Turning our attention to the observed values for the separation between the bottom of the adatom band and the two adatom peaks, 0.099 ± 0.017 V and 0.265 ± 0.022 V, these values will be shifted only slightly by the tip-induced band bending (since the semiconductor is in accumulation). We deduce corrections of -0.01 ± 0.01 V and -0.025 ± 0.025 V, respectively, relative to the bottom of the adatom band. We thus assign values of 0.09 ± 0.02 eV and 0.24 ± 0.03 eV to the respective peak positions relative to the bottom of the adatom band, and a value of 0.15 ± 0.03 eV to the separation between the peaks.

C. Interband current

In addition to computational results for surface band bending, an additional important quantity to consider is the sample voltage at which inversion of the surface electronic states occurs. The situation is pictured in Fig. 10, where we consider a *p*-type semiconductor in depletion. When the magnitude of the surface band bending, $|f_0|$, exceeds the band gap of the semiconductor, then carriers can tunnel from VB to CB through the semiconductor band gap. If this *interband current* is sufficiently large, then the CB states will be occupied up to the Fermi-level and inversion of the semiconductor is said to occur. The question of how large this interband current need be to produce inversion is a nontrivial one and, in principle, requires detailed knowledge of a number of transport processes. However, if the transport of the carriers in the semiconductor after they tunnel from VB to CB is relatively fast, then a condition for establishing inversion is simply that

$$I_S \geq I_V \tag{8}$$

where I_S is the interband tunneling current in the semiconductor and I_V is the tunneling current in the vacuum.

It is clear that the dominant term in establishing the interband current is the transmission through the band gap. This term has been considered by Jäger *et al.* [23], where they find that for GaAs, with band gap of about 1.4 eV, the interband transmission is negligible compared to the transmission through the vacuum, at least for sample-tip voltage that are not too large. However, for smaller band gaps, the interband transmission and the associated interband current can approach or exceed those values for the vacuum. We compute interband tunneling in 3-D, using the method described in Appendix III. The transmission of the carrier through the band gap region of the semiconductor is described using the two-band model for the complex band structure in the band gap [24], (*i.e.* with the inverse decay length of the wavefunction having a maximum value at midgap and approaching zero as the energy approaches either band edge), and using an effective mass of $0.043\, m_0$ corresponding to the light-hole mass of the Ge VB [25]. Figure 10 shows the resulting interband currents as computed for semiconductors with various values of the band gap and for a tip radius of 100 nm. As expected the interband currents show a dramatic reduction as the band gap increases. Interband currents on the order of the vacuum tunneling current (≈ 0.1 nA) occur only for the 0.5 eV band gap case. The inset of the figure shows the dependence of the interband current on tip radius, for a particular sample voltage of -2 V . We find a broad maximum in this dependence; for sharp tips the interband current is small because the tip-induced band bending is small, whereas for blunt tips the band bending is large but the associated depletion region extends a greater distance into the semiconductor and hence the interband current is again relatively small.

To compare our computed interband currents with the experimental results for the Ge(111)c(2×8) surface we must consider the possibility of carriers tunneling through

the depletion region from the bulk VB into the *surface band* of adatom states, *e.g.* as pictured in Fig. 8 by the current I_S. Our method for computing the interband current is also applicable to this case, albeit in an approximate manner as discussed at the end of Appendix III. The resulting values for the interband current for the Ge(111)c(2×8) surface are very close to the 0.5 eV band gap results of Fig. 10. Examining in particular the results in the inset, for a sample voltage of -2 V, we see that the computed current achieves values of ≈ 0.1 nA consistent with our experiments only when the tip radius has a value of roughly 100 nm. This result does not change significantly even when a surface defect state density of about 3×10^{12} cm^{-2}eV^{-1} is included.

Based on the condition expressed by Eq. (8) the approximate agreement between theoretical and experimental inversion currents for the tip radius of 100 nm would imply that this value is characteristic of the probe tip used in our experiments. Smaller values, such 10 nm, might also be allowed if the transport through the semiconductor is slow (*i.e.* if Eq. (8) is not appropriate), but radii as small as 1 nm seem rather unlikely based on the observed inversion voltages. These conclusions are consistent with prior experience in STM, where tip radii of 10 - 100 nm are typically found by field emission measurements on tips produced by a wide range of preparation conditions [11,26,27]. Sharper tips with radii less than 10 nm are possible, but only for exceptional preparation conditions. Somewhat blunter tips are also possible, although the known occurrence of small nm-scale protrusions at the end of the tip – as seen directly seen in field emission microscopy images and also evidenced by the atomic-scale resolution commonly achieved in STM images – would argue against having average *effective* tip radii that are overly large.

D. Rest-atom peak shift

Based on the previous section, it seems reasonable to focus our attention on probe tips with radii in the range of 10 - 100 nm. Using these radii let us then consider how the density of surface disorder-induced states might affect the observed position of the rest-atom peak. In the limit of very low tunnel currents, we expect equilibrium between the occupation of surface and bulk states. Also, as the temperature increases, hopping between surface states (intrinsic or extrinsic) will increase and transfer between surface and bulk states by various mechanisms should also increase. Thus, an equilibrium situation, with $E_F = E_{F,S}$ as pictured in Figs. 11(a) and (b), is expected for low currents and high temperatures. Referring to our data in Fig. 6, the 61 K data at the lowest current values is expected to be the situation closest to equilibrium. We observe a rest-atom peak at 0.9 V below the VB maximum in this case, which can be compared to the known position of the rest-atom band is at $E_V - 0.7$ eV. Assuming zero contact potential this comparison would imply a band bending of about 0.2 eV, or slightly more or less than that if a nonzero contact potential existed in the experiment. To compare the experimental results for the rest-atom peak position with experiment we compute band bending for a range of sample voltages, and search for the voltage at which the rest-atom state is aligned with the tip Fermi-level.

Theoretical results are shown in Fig. 6, for tip radii of 10 and 100 nm. The equilibrium results there refer to the case of a surface Fermi-level equal to the bulk Fermi-level, $E_{F,S}(r) = E_F$. The predicted variation of rest-atom position with sample-tip separation is relatively small, and much less than the observed variation in the peak positions at any given temperature. We have assumed values of the contact potential Δf of 0.0 and $+0.3$ eV for the 10 and 100 nm results, respectively, in order to approximately align the equilibrium results with the observations at low current and high temperature (a contact potential of 0 for the 100 nm case causes the line to shift downwards by 0.2 - 0.3 eV, as seen in Fig. 3 of our prior work [18]). We note that the expected contact potential difference between a clean, unpinned Ge(111) surface and a Cu(111) surface is about 0.0 eV [28,29], although the precise condition of the probe-tip used in our experiments is unknown. In any case these assumed values for the contact potential do not impact any of our main conclusions below.

The equilibrium theory is seen to disagree with the full range of the data in Fig. 6, a result that relies on the validity of the theoretical computations. We have tested this validity by taking the solution for the electric-field distribution and then solving the *inverse* problem using the method of images, as described in Appendix I. Equality between the inverse solution and the original boundary condition is obtained. In particular, the relatively slow variation of tip-induced band bending with sample-tip separation reflected in Fig. 6 is an essential feature of the 3-D semiconductor-vacuum-metal electrostatic problem (see, *e.g.*, Fig. 5 of Ref. [19]). For separations greater than about 4 Å, and for the tip radii considered here, the variation of surface potential with separation is relatively small. As discussed in Section III(D) we are confident that any experimental uncertainty in the zero of sample-tip separation will lead only to an *increase* in the separation values shown in Figs. 5 and 6, not a decrease.

Now let us consider the experimental results for high current and/or low temperature. In this case a large shift of the rest-atom peak position is found, implying the presence of some non-equilibrium surface charge [18]. We propose that the occupation of the extrinsic disorder-induced surface states are *not* in equilibrium with the bulk, so that they are the origin of the excess surface charge. The situation is pictured in Figs. 11(c) and (d). In this case, with negative sample-tip voltage, we assume that the surface Fermi-level is below the bulk Fermi-level. In the extreme case that the surface states are totally depleted of charge then the surface Fermi-level is equal to the surface VB maximum, $E_{F,S}(r) = E_{V,S}(r) \equiv E_V + f(r,0)$. We assume that this situation holds for radii less then some critical value, and for larger radii we again have $E_{F,S}(r) = E_F$. Using a critical radius of 300 nm, theoretical results for this non-equilibrium case are shown in Fig. 6. We see that the expected rest-atom peak positions are indeed shifted in the theory, by amounts that approximately bring them into agreement with the data on the high current side of the graph. Within our model for nonequilibrium occupation of the extrinsic states, we would thus envisage the rest-atom peak position shifting from the equilibrium results on the left-hand side of Fig. 6 to the nonequilibrium results on the right-hand side of the graph, and thus an approximate agreement between theory and experiment would be obtained.

There are two arbitrary parameters in our model of nonequilibrium occupation – the degree of depletion of the disorder-induced states in the presence of the hole-injecting tunnel current, and the radius over which this effect extends. Actually these two parameters are coupled, since we could have assumed less depletion of the midgap states over a larger radius (and/or increased the number of states within the range consistent with the STM images) and achieved similar results. To justify the value of either or both of these parameters is not possible at present, since it would require detailed knowledge of (i) the hole concentration near the surface, (ii) the recombination rate of holes in the midgap states, (iii) reoccupation rate for those states by electrons tunneling through the semiconductor depletion region, and (iv) the transport rate for hopping of carriers between the disorder-induced states. Process (iii) can be quantified in a manner similar to the interband current discussed in the previous section, and some aspects of item (i) are discussed below, but little is known at present about the other transport processes. However, even though our model is not parameter free, we argue below that it is the most likely possibility when compared with other conceivable sources of nonequilibrium charge, namely, accumulation of holes in near-surface bulk states or in the rest-atom states of the c(2×8) reconstruction.

Regarding accumulation of holes in bulk states, the density of holes in the VB can be estimated from the known tunnel current. Holes injected in the VB, although they traverse the vacuum with a relatively narrow range of angles relative to the central axis (due to the well known dependence of the vacuum transmission barrier on parallel wavevector), will greatly spread out upon entering the semiconductor [30]. Scattering of these ballistic holes occurs primarily by emission of LO-phonons (scattering length about 30 nm) and by acoustic phonons (scattering length about 300 nm) [31]. The trajectories of injected ballistic holes will be bent away from the surface due to the electric field in the Ge, but until the holes are fully thermalized this should not be a large effect. To estimate a hole concentration p, we can use the relationship for the current density $J = pev$ where v is the drift velocity. For thermalized holes we can take $v = \mu E$ with mobility μ and electric field E. Thus, considering an injected current of 1 nA over the surface of a half-sphere with radius of 100 nm, using a field of ≈ 0.01 V/nm from our computations, and with a bulk mobility of about 10^4 cm^2/Vs [32], the resulting hole density is 1×10^{13} cm^{-3}. This value is much less than the space charge density of 2×10^{16} cm^{-3} in the depletion region, so its effect on the potential distribution will be negligible. Using a radius of 10 nm in the above estimate, and a field from the computations of ≈ 0.1 V/nm, the hole density would be 1×10^{14} cm^{-3} which is still less than the space charge density (and at this radius the velocity should also be higher, since the hole transport would be largely ballistic). We conclude that it is unlikely that bulk-limited transport, *i.e.* a bulk spreading resistance type of effect, could account for our observations (although it could well be an important factor at current levels one or two orders-of-magnitude higher than that used in our experiments).

Two other factors argue against the role of bulk transport in our experiments. First, our observed temperature dependence in which the transport effects become more pronounced as the temperature *decreases* is contrary to the usual *increase* in bulk mobility with decreasing temperature. For an effect arising from the disorder-induced states, however, temperature-dependent hopping between the states would have an appropriate temperature dependence [2], as further discussed below. Secondly, the observed rest-atom peak shift varies only very slowly, approximately logarithmically, with current [18]. For an effect arising from bulk transport we would expect more of a linear turn-on for currents above some critical value. Alternatively, for a band of disorder-induced states, increasing the occupation of the band (*i.e.* with holes in this case) would lead to an increased intraband conductivity thereby promoting equilibration within the band, so that an increasing tunnel current would only *slowly* increase the occupation of the band and the concomitant shift of the rest-atom peak.

Let us now consider the possible role of the band of c(2×8) rest-atom states. First, it is important to recall that these states are resonant with the VB, so any holes occupying those states would be expected to rapidly dissipate into VB states. Nevertheless let us ignore that effect for a moment, and consider the possible transport of holes within the rest-atom band itself. If this transport was limited, then one could envision a buildup of positive charge during the STS measurement at negative sample voltages. However, in that case we would expect an analogous effect for the transport of electrons through the adatom-states, for positive sample voltages. As described in Section III(C), we do *not* observe any such effects at positive sample voltages, to a relatively high degree of accuracy (*e.g.* see Figs. 4(a) - (c)). And again, since the rest-atom states are degenerate with the VB we would expect that, if anything, transport through these combined VB/rest-atom states to be much faster than for the adatom states. One additional observation also argues against the role of rest-atom states in the transport limitation: in the temperature-dependent spectra (Fig. 2 of Ref. [18]), the shifting rest-atom feature does *not* get broader as it shifts, but rather it maintains a constant width and simply moves to more negative voltages. If these rest-atoms state themselves were solely responsible for the limited transport then we believe that this peak should exhibit significant broadening as it shifts.

We have considered a number of alternate models for the shifting rest-atom spectral feature, most notably the possible influence of the electric field at the surface. This field has magnitude in the range 0.1 - 0.2 V/Å for the relevant sample-tip voltages and separations. Since the energy splitting between adatom and rest-atom states depends on the charge transfer between these species, a modification of this charge transfer due to the field must be considered, especially since changes in this charge transfer *are* commonly observed in surface adsorption reactions [33]. Indeed, for negative sample-tip voltages the field will induce charge transfer from rest-atom to adatom thereby lowering the energy of the rest-atom state, consistent with our observations. However, to fully account for our data the shift of the rest-atom state with field would have to be quite large, similar to that estimated for the extreme case of alkali-metal adsorbates [34], and furthermore the shift would have to vary quite nonlinearly with field to follow the data of Fig. 6.

Our main argument against an explanation based on electric field is that it is difficult to envision any temperature dependence for this mechanism. Our data does show clear temperature dependence, as in Fig. 6, in agreement with the prior results of Dujardin *et al.* [2]. Within our model of nonequilibrium extrinsic-state occupation we believe that this temperature dependence arises from temperature-dependent hopping between the states. At high temperature this transport process is relatively rapid, producing equilibrium occupation of the states. But at low temperature and high current the process is slow compared to the supply rate of holes from the tunnel current, producing nonequilibrium extrinsic state occupation. We emphasize that the extrinsic states are present on the surface both at high and low temperatures but within our model it is their occupation, under conditions of injected hole current, that varies with temperature.

V. Conclusions

In summary, we have identified features in low-temperature tunneling spectra acquired from *p*-type Ge(111)c(2×8) surfaces associated with the VB maximum, with surface rest-atom and adatom bands, and with the occurrence of inversion of the surface electron occupation. A bulk band gap of 0.5 ± 0.1 eV is determined. The spectral position of the rest-atom peak is found to shift considerably with current and/or temperature. This shift was discussed in our prior work, where we argued that some additional, non-equilibrium source of positive charge at or near the surface was likely responsible for it [18]. We have demonstrated in the present work that a possible source of this surface charge are disorder-induced states associated with the disordered arrangements of adatoms occurring at domain boundaries of the c(2×8) structure. We find that our observed results for the rest-atom peak position can be well understood by including a density of disorder-induced states which is consistent with that observed in the STM images, and assuming that such states are significantly depopulated by holes injected due to the tunneling current.

We believe that the model proposed here provides a likely explanation not only for our results but also for the prior results of Dujardin *et al.* [2]. The temperature dependence of the results would arise from temperature-dependent hopping, a mechanism identified in the work of Dujardin *et al.* Those workers were not specific, however, in distinguishing between hopping between intrinsic states of the c(2×8) surface or between extrinsic disorder-induced states. We believe it is the latter that is responsible for the observed effects, as argued in Section IV(D). We briefly mention in this regard the previous work on the SiC(0001) $\sqrt{3}\times\sqrt{3}$ - $R30^\circ$ surface in which current-dependence of the spectra was also observed, but for which it seems quite clear that it is the *intrinsic* states of the reconstructed surface which produce the transport limitations [4]. One difference between that system compared to Ge is the much larger band gap for SiC (2.9 eV), yielding vastly smaller tunneling rates for carriers through the depletion region of the semiconductor. Also, the dangling bonds of the SiC adatoms are quite localized, producing Mott insulator behavior for that system [4,35]. Further study is needed to more fully understand the difference between this case as compared to the Ge surface.

Our model can also be compared with that previously described by Ono *et al.* [3] as a possible explanation for the low-temperature results first observed by Takayanagi and co-workers on the Si(001) surface [1]. Although the experimental situations (and findings) are quite different than for the Ge(111)c(2×8) surface, we do feel that there is one significant similarity between the two cases. Specifically, for the temperature dependence of the Si(001) STM images, Ono *et al.* proposes that the current originating from occupation of the normally empty p^* surface band can account for the observations. As to why this current should vary with temperature, *i.e.* why the Fermi-level moves up into this band as the temperature is reduced, those workers suggested the freeze-out of free carriers (increased Debye length) could be responsible. On this latter point we suggest that an alternative explanation can be found be considering the occupation of midgap defect and/or disorder-induced states (some of which invariably occur on Si(001) surfaces). At elevated temperatures these states will act to pin the Fermi-level near midgap, *i.e.* below p^* band, but at low temperatures the states may be out of equilibrium with the bulk and the surface Fermi-level could then move into the p^* band.

Finally, we briefly comment on the implications of this work for STS measurements of semiconductor surfaces in general. The possible occurrence of tip-induced band bending (for surfaces possessing a band gap) has been known from the early days of STS [5], and it is well known that use of high doping concentrations and/or sharp probe tips will minimize such effects [11]. The dependence of tip-induced band bending on current and temperature has not, however, been previously considered. In particular, nonequilibrium effects in the occupation of midgap states can produce, as argued in this work, potentially important effects both STS and STM measurements of semiconductor surfaces at low temperature and/or high current levels. However, for measurements at room temperature, with low currents, such effects in many cases should be small and the regular equilibrium theory should generally suffice to estimate the effects of tip-induced band bending on tunneling spectra.

Acknowledgements

Discussions with G. Dujardin, J. E. Northrup, and M. Widom are gratefully acknowledged. This work has been supported by the A. Von Humboldt Foundation and by the U.S. National Science Foundation.

Appendix I - Finite-element computation of electrostatic potential

We have made two extensions to our finite element method for solving Poisson's equation relative to the theory presented in Ref. [19]. First, as discussed in Section IV(A), we allow for the presence of a surface charge density within the boundary condition of Eq. (5). Following in detail the definitions and notation of Ref. [19] this boundary condition, in a first-order approximation, takes the form

$$\frac{\left(f_{i,1}^{V}-f_{i}\right)}{ax_{i}\Delta h}=e\frac{\left(f_{i}-f_{i,1}^{S}\right)}{\Delta z}+\frac{es\left(E_{F,S}-f_{i}\right)}{e_{0}} \quad . \tag{A1.1}$$

where the subscript i refers to the ith radial grid point, f_i is the potential on the surface, $f_{i,1}^{V}$ is the potential at the first grid point in the vacuum located at a distance of $ax_i\Delta h$ from the surface, and $f_{i,1}^{S}$ is the potential at the first grid point in the semiconductor located at a distance of Δz from the surface. This equation can be rearranged to yield the surface potential

$$f_{i}=\frac{\dfrac{f_{i,1}^{V}}{ax_{i}\Delta h}+e\dfrac{f_{i,1}^{S}}{\Delta z}-\dfrac{es\left(E_{F,S}-f_{i}\right)}{e_{0}}}{\dfrac{1}{ax_{i}\Delta h}+\dfrac{e}{\Delta z}} \quad . \tag{A1.2}$$

Taking the quantities $f_{i,1}^{V}$, $f_{i,1}^{S}$, and f_i on the right-hand side of this equation to have their values at the kth iteration, we can then evaluate the right-hand side to obtain f_i at the (k+1)st iteration. Let us call this value $\tilde{f}_i^{(k+1)}$. We find that for large, nonlinear surface charge density this method for updating f_i can lead to instabilities in the iterative solution. An analogous problem was encountered in our bulk solution of Poisson's equation [19], and we formulate here a similar solution to the problem as used for the bulk: We take the f_i on both the right- and left-hand sides of Eq. (A1.2) to be the values at the (k+1)st iteration, and we solve the equation implicitly for this value. To accomplish this we perform a 1-D search, using as limits $\tilde{f}_i^{(k+1)}$ and $f_i^{(k)}$ [36]. With this method we obtain a stable iterative solution for the potential. One final comment regarding the boundary condition is that we actually use a third-order solution for this, rather than the first-order form of Eq. (A1.2), thereby obtaining substantially improved convergence of the iterative finite-element method.

The second extension to our finite-element theory is the use of a grid with variable spacing in both the r- and z-directions. Given the parameters Δr and Δz, the grid points in the radial direction are taken to be

$$r_i = \frac{2M\Delta r}{p}\tan\left(\frac{p\,(i-0.5)}{2M}\right) \qquad i = 1,2,3,\ldots,M \tag{A1.3}$$

and in the *z*-direction into the semiconductor by

$$z_j = -\frac{2N\Delta z}{p}\tan\left(\frac{p\ j}{2N}\right) \qquad j = 1,2,3,\ldots,N-1 \quad . \tag{A1.4}$$

The spacing between grid points as used in finite-element formulae for derivatives are then given by

$$\Delta r_i = \Delta r\,\cos^{-2}\left(\frac{p\,(i-0.5)}{2M}\right) \tag{A1.5}$$

and

$$\Delta z_j = -\Delta z\,\cos^{-2}\left(\frac{p\ j}{2N}\right) \quad . \tag{A1.6}$$

This variable grid spacing is found to be particularly useful in problems involving low-doped semiconductors and relatively sharp tips, for which a small grid spacing near the tip apex is needed but a large total extent for the simulation is also required.

In addition to the above two extensions of our finite-element theory, we have also undertaken a validation of the computer program that implements the technique. To accomplish this we take the output of the program and then use that in a separate (small) computer program to solve the *inverse problem*. The output of the original program provides the electrostatic potential energy $f(r,z)$ at every point in space. Of specific interest is the surface charge density on the probe tip, which is obtained from $s_T = e_0 E_n$ where E_n is the electric field normal to the surface of the tip as given by $|\nabla f|/e$. We consider for simplicity a situation with zero-doping in the semiconductor, in which case this surface charge is the *only* charge in the problem. In this case, the inverse problem can be solved simply by taking this surface charge density and integrating it to obtain the potential at any point in space. We use the method of images [37] to perform this integration for our system containing the dielectric in a half-space, so that the potential energy at any point in space is given by

$$f = \int \frac{s_T\,dA}{R} + \int \frac{s_T'\,dA}{R'} \tag{A1.7}$$

with the integrals extending over the surfaces of the tip and its mirror image in the dielectric, respectively, the distances R and R' are defined in the inset of Fig. 12, and where

$$s'_T = -\left(\frac{e-1}{e+1}\right) s_T \quad . \tag{A1.8}$$

Figure 12 shows a comparison between the solution for the inverse problem and the original problem, plotting the results as a function of the number of grid points used for both solutions (this same number of points is used in both the *r*- and *z*-directions). The original problem converges quite quickly to the final solution. The inverse problem requires a much finer grid to achieve the same solution (this finer grid to needed to accurately describe the potential over the entire surface of the probe-tip including out to large distances from the surface as achieved with our variable grid spacing) but equality between the two solutions, within 0.5%, is finally achieved.

Appendix II - Self-consistent treatment of accumulation layer states

To test the validity of the semi-classical results discussed in the main text of this paper, we describe here a self-consistent, quantum-mechanical treatment of band bending for the case of accumulation (a similar treatment would also hold for inversion). In the 3-D confining potential of the accumulation region the localized wavefunctions are denoted by $\Psi_j(r,q,z)$ with energies E_j, and where we are using cylindrical coordinates (r,q,z) with $z<0$ in the semiconductor. To be specific we consider the case of *p*-type material with positive sample voltage, so that the only charge density in the semiconductor that need be considered is that arising from the occupation of the VB by holes. The potential is computed from Poisson's equation in a Hartree manner, with the charge density being obtained from

$$r(r,q,z) = 2e\sum_j \left[1 - f(E_j)\right] \left|\Psi_j(r,q,z)\right|^2 \qquad \text{(A2.1)}$$

where $f(E_j)$ is the Fermi-Dirac occupation factor for the state with energy E_j, and the factor of 2 is for spin degeneracy.

We assume a large barrier in the vacuum, such that the amplitude of the wavefunction at the semiconductor surface is zero. The wavefunction for localized states are described in separable form as $\Psi(r,f,z) = cR(r)\Theta(q)Z(z)$ where *c* is a normalization factor. With azimuthal symmetry, $\Theta(q) = \exp(imq)$ where $m = 0,\pm1,\pm2,\ldots$ is the azimuthal quantum number. In the radial direction we use as a basis set wavefunctions of the 2-D harmonic oscillator,

$$R(r) = r^{|m|} L_n^{|m|}\left(\frac{mwr^2}{\hbar}\right)\exp\left(-\frac{mwr^2}{2\hbar}\right) \qquad \text{(A2.2)}$$

where $L_n^{|m|}$ is an associated Laguerre polynomial with radial quantum number $n = 0, 1, 2,\ldots$, and where $m = m_{dh}$ is the hole effective-mass and w describes the radial-curvature of the potential at the origin as specified below. In the *z*-direction we use Airy functions (*i.e.* appropriate to a triangular potential),

$$Z_i(z) = \mathrm{Ai}\left(-\left(\frac{2meF}{\hbar^2}\right)^{1/3} z + a_i\right) \qquad \text{(A2.3)}$$

where $a_i < 0$ are the zeroes of the Airy function and *F* is the electric field in the semiconductor at the origin. For these wavefunctions, the normalization constant *c* is evaluated to be

$$c_{inm} = \sqrt{p}\left(\frac{\hbar^2}{2meF}\right)^{1/6} \mathrm{Ai}'(a_i)\left(\frac{\hbar}{mw}\right)^{(|m|+1)/2} \sqrt{\frac{(|m|+n)!}{n!}} \qquad \text{(A2.4)}$$

where $\mathrm{Ai}'(a_i)$ are derivatives of the Airy function evaluated at its zeroes.

We use a first-order perturbation treatment to evaluate the wavefunctions and resulting charge density. For the zeroth-order wavefunctions we use the forms given by Eqs. (A2.2) and (A2.3), in which the parameters w and F are evaluated from $mw^2 = \partial^2 f / \partial r^2$ and $eF = \partial f / \partial z$ where $f(r,z)$ is the potential energy and the derivatives are evaluated at the origin. We evaluate these derivatives using a Gaussian fit to $f(r,0)$ and an exponential fit to $f(0,z)$, respectively. Our approach thus follows that used by Dombrowski *et al.* [27], except that in our case we obtain the potential by a full 3-D solution to Poisson's equation whereas those workers assumed a Gaussian form for the potential with parameters chosen to match experiment.

At each iteration of the computation, new values for the potential are evaluated according to our finite-element scheme described in Appendix I, and from that potential we obtain new values of w and F. According to the above choice of wavefunctions the zeroth-order potential is taken to be parabolic in the r-direction and triangular in the z-direction ($z < 0$), with energies for these hole states given by

$$E_{inm}^{(0)} = -\hbar w\left(2n + |m| + 1\right) - \left(\frac{\hbar^2}{2m}\right)^{1/3} (eF)^{2/3}|a_i| + f(0,0) \qquad \text{(A2.5)}$$

where the first-term is from the 2-D harmonic oscillator wavefunctions, the second term from the Airy functions, and the third term provides a zero reference value for the energies. First-order correction to these energies are then given by

$$\Delta E_{inm} = \left\langle \Psi_{inm} \middle| f(r,z) + \frac{1}{2} mw^2 r^2 - eFz - f(0,0) \middle| \Psi_{inm} \right\rangle \quad . \qquad \text{(A2.6)}$$

The perturbing potential listed here, while suitably small near the origin, actually diverges at large values of r or z. However this is not a problem in the evaluation of the integral since the wavefunctions decay exponentially as a function of r or z, thus producing finite (and small) values for ΔE. This integral is evaluated for ascending values of i, n, and $|m|$ until $E_{inm}^{(0)} + \Delta E_{inm}$ is several kT below E_F, and the entire set of wavefunctions thus obtained are then used in Eq. (A2.1) to evaluate the new charge density.

Results are shown in Fig. 13 for the band bending under accumulation conditions as a function of sample voltage, comparing the semi-classical results with the quantum results and using the same effective mass of $0.35\,m_0$ [from Section IV(A)] in both cases. We

also indicate the number of quantum states occupied at zero temperature for various points along the curve. (One might expect the solid curve to have discontinuities as the number of states changes, but in our self-consistency loop the occupations oscillate between neighboring integers thus yielding, in effect, fractional occupation of the states and a continuous result for Fig. 13). The semi-classical results are seen to provide a rather good estimate of the band bending, despite the fact that the charge densities in the two cases are quite different as seen in the insets of Fig. 13. As seen there for the charge density r as a function of z along the central axis, the quantum treatment produces only a single state in the z-direction, for the value of effective mass used here.

Appendix III - Tunneling in a spherical geometry

The expressions for planar tunneling as derived within the WKB approximation are well known [38]. Our goal in this Appendix is to develop an analogous formalism for computing an interband tunnel current in a nearly spherical geometry. We consider traveling waves incident on the semiconductor depletion region as pictured in Fig. 14. So long as the energy of those waves is greater than $E_C + f_0$ (with $f_0 < 0$) then those waves can tunnel through the band gap region and contribute to the interband current. For ease of discussion we initially assume that, within the semiconductor, the equipotential curves have perfect spherical symmetry relative to an origin located at some point $z = z_0 > 0$ along the central axis. In terms of the spherical coordinates (R, Θ, Φ), the appropriate wavefunction for the incident electrons is the linear combination of plane waves that carries current only towards the origin [39],

$$y_{\ell m}(R, \Theta, \Phi) = C_\ell \, h_\ell^{(2)}(kR) \, Y_\ell^{\,m}(\Theta, \Phi) \tag{A3.1}$$

where ℓ and m are angular momentum quantum numbers, $Y_\ell^{\,m}$ is a spherical harmonic, $h_\ell^{(2)}$ is a spherical Hankel function of the second kind, and $k = \sqrt{2m^* E}/\hbar$ where E is the energy of the state and m^* is an effective mass. The spherical Hankel function consists of a power series in inverse powers of R, multiplied by an exponential term $\exp(-ikR)$. So long as a nonzero size region near the origin is excluded, which is the case for our problem, then these wavefunctions can be normalized, resulting in $C_\ell = k/\sqrt{R_m}$ where R_m is the maximal radius of the semiconductor.

The current carried by each incident wave is $e\hbar k/(m^* R_m)$. Summing over all incident waves, and including a factor of 2 for spin degeneracy, we arrive at the expression for the total interband current

$$I_S = \frac{2e}{h} \int_{E_C + f_0}^{E_V} dE \, \frac{\Omega(E)}{4p} \, f(E) \sum_{\ell=0}^{\infty} (2\ell + 1) \, D_\ell(E) \tag{A3.2}$$

where $D_\ell(E)$ is the transmission of an incident wave through the band gap and $f(E)$ is the occupation of the incident VB state. $\Omega(E)$ is the solid angle subtended by the surface through which the current flows, *i.e.* the area of that surface divided by its radius of curvature squared. With spherical symmetry the transmission can be estimated using the WKB approximation in 3-D [40],

$$D_\ell(E) = \exp\left\{ -2 \int_{R_1}^{R_2} \left[\frac{2m^*}{\hbar^2} \Delta E_b + \frac{\ell(\ell+1)}{R^2} \right]^{1/2} dR \right\} \tag{A3.3}$$

where ΔE_b is the barrier seen by the electrons, and R_1 and R_2 are the turning points *i.e.* the values of R for which the integrand is zero. The barrier seen by the electron varies from 0 when E coincides with the VB maximum or CB minimum, up to a maximum value when E is near midgap, in accordance to the complex band structure of the

material. We use the well-known two-band model of Kane [24], for which the barrier can be expressed as [41]

$$\Delta E_b = \left[E - E_V + \hat{f}(R)\right] - \frac{\left[E - E_V + \hat{f}(R)\right]^2}{E_G} \qquad \text{(A3.4)}$$

where E_V and E_C are the VB maximum and CB minimum, respectively, at a point far inside the semiconductor, $E_G = E_C - E_V$ is the band gap, and $\hat{f}(R) \equiv f(0, z_0 - R)$.

Equations (A3.2) - (A3.4) permit evaluation of the interband current for a spherically symmetric geometry. To extend this theory to situations that deviate slightly from spherical symmetry we compute the transmission factors by taking line integrals along the electric-field lines pictured in Fig. 14. Along the *i*th such line we introduce an integration variable a_i. The value of $R(a_i)$ at each point along these integrals is taken to be the local value of the radius of curvature of the equipotential, $R_C(a_i) = \left(\partial^2 r_f / \partial z^2\right)^{-1}$ where $r_f(z)$ is the equipotential curve for the particular value of f at the location a_i along the electric-field line (we are using the same (r, z) cylindrical coordinates here as introduced in Section IV). To obtain the contribution to the total current from each such transmission factor, we evaluate the fraction the solid angle subtended by the contribution to the current from the integration along the *i*th electric field line (we evaluate this solid angle according to the local values of radius of curvature at the outer surface of the tunneling region, *e.g.* the -0.1 eV contour in Fig. 14).

One remarkable feature of the above WKB result for the tunnel current, Eq. (A3.2), is that it is independent of the details of the final states into which the current flows (i.e. this state must exist, but its amplitude does not enter into the formulas for the current). This independence occurs because the WKB formalism as used here neglects detailed matching of the wavefunction across the turning points. This procedure is clearly an approximation, but in most cases it should be a good one since the transmission factor is dominated by exponentially small terms associated with the barrier height and width whereas the amplitude of the wavefunction will only introduce linear corrections to this result. For the present case of interest of estimating inversion currents for the Ge(111)c(2×8) surface we therefore need only identify the relevant energies to be used in the equations. For the band gap in the barrier height, Eq. (A3.4), we must use the full band gap of Ge, $E_G = 0.74$ eV. However in the energy integral of Eq. (A3.2), the value of the conduction band minimum in the lower limit of the integral will be that given by the *surface* band gap, for which we use the value of 0.5 eV as determined in Section IV(B).

References:

[1] T. Yokoyama and K. Takayanagi, Phys. Rev. B **61**, 5078 (2000); T. Mitsui and K. Takayanagi, Phys. Rev. B **62**, R16251 (2000).
[2] G. Dujardin, A. J. Mayne, and F. Rose, Phys. Rev. Lett. **89**, 036802 (2002).
[3] M. Ono, A. Kamoshida, N. Matsuura, E. Ishikawa, T. Eguchi, and Y. Hasegawa, Phys. Rev. B **67**, 201306(R) (2003).
[4] V. Ramachandran and R. M. Feenstra, Phys. Rev. Lett. **82**,1000 (1999).
[5] R. M. Feenstra and J. A. Stroscio, J. Vac. Sci. Technol. B **5**, 923 (1987).
[6] R. S. Becker, B. S. Swartzentruber, J. S. Vickers, and T. Klitsner, Phys. Rev. B **39**, 1633 (1989).
[7] F. J. Himpsel, Surf. Sci. Rep. **12**, 1 (1990).
[8] R. M. Feenstra and A. J. Slavin, Surf. Sci. **251/252**, 401 (1991).
[9] G. Meyer, Rev. Sci. Instrum. **67**, 2960 (1996).
[10] R. M. Feenstra, G. Meyer, F. Moresco, and K. H. Rieder, Phys. Rev. B **64**, 081306(R) (2001).
[11] R. M. Feenstra, Phys. Rev. B **50**, 4561 (1994). There is a typographical error in Eqs. (4) and (5), they should be multiplied by a normalization factor of $1/(2?V)$.
[12] P. Mårtensson and R. M. Feenstra, Phys. Rev. B **39**, 7744 (1989).
[13] E. S. Hirschorn, D. S. Lin, F. M. Leibsle, A. Samsavar, and T.-C. Chiang, Phys. Rev. B **44**, R1403 (1991).
[14] N. Takeuchi, A. Selloni, and E. Tosatti, Phys. Rev. Lett. **69**, 648 (1992).
[15] J. Aarts, A. J. Hoeven and P. K. Larsen, Phys. Rev. B **37**, 8190 (1988), and references therein.
[16] C. B. Duke, *Tunneling in Solids* (Academic Press, New York, 1969), Eq. (7.8).
[17] Y. Dong, R. M. Feenstra, M. P. Semtsiv, and W. T. Masselink, submitted to J. Appl. Phys.
[18] R. M. Feenstra, G. Meyer, K.-H. Rieder, Phys. Rev. B **69**, 081309(R) (2004).
[19] R. M. Feenstra, J. Vac. Sci. Technol. B **21**, 2080 (2003).
[20] H. Hasegawa and H. Ohno, J. Vac. Sci. Technol. B **4**, 1130 (1986); W. E. Spicer, I. Lindau, P. Skeath, C. Y. Su, and P. Chye, Phys. Rev. Lett. **44**, 420 (1980); J. Tersoff, J. Vac. Sci. Technol. B **3**, 1157 (1985).
[21] S. M. Sze, *Physics of Semiconductor Devices* (Wiley, New York, 1969), p. 27.
[22] *Semiconductors: group IV elements and III-V compounds*, ed. O. Madelung, (Springer-Verlag, Berlin, 1991).
[23] N. D. Jäger, E. R. Weber, K. Urban, and Ph. Ebert, Phys. Rev. B **67**, 165327 (2003).
[24] E. O. Kane, J. Chem. Phys. Solids **12**, 181 (1960).
[25] Within the two-band model the effective mass m^* has a single, fixed value. In principle a more complicated model should be used to allow m^* to vary as the energy moves from E_V to E_C, but for the present case the dominant contribution to the integral of Eq. (A3.3) arises from energy values are in the lower portion of the band gap so that our use of the light-hole mass of the Ge VB is a good approximation.
[26] Y. Dong, R. M. Feenstra, R. Hey, and K. H. Ploog, J. Vac. Sci. Technol. B **20**, 1677 (2002).
[27] R. Dombrowski, Chr. Steinebach, Chr. Wittneven, M. Morgenstern, and R. Wiesendanger, Phys. Rev. B **59**, 8043 (1999).

[28] G. W. Gobeli and F. G. Allen, Surf. Sci. **2**, 402 (1964).
[29] Q. Zhong, C. Gahl, and M. Wolf, Surf. Sci. **496**, 21 (2002).
[30] This spreading is most easily understood within a planar tunneling model where it is a direct consequence of satisfying both energy and parallel wavevector conservation (analogous to that occurring in ballistic-electron-emission microscopy, see L. D. Bell and W. J. Kaiser, Phys. Rev. Lett. **61**, 2368 (1988)), but will also occur for the more spherical geometry of a sharp probe tip.
[31] D. Sprinzak, M. Heiblum, Y. Levinson, and H. Shtrikman, Phys. Rev. B **55**, R10185 (1997). Scattering lengths in this work are for low-doped GaAs at low temperatures. Values for Ge will be somewhat larger due to its smaller light-hole mass.
[32] J. Singh, *Physics of Semiconductors and their Heterostructures* (McGraw-Hill, New York, 1993), Fig. 11.6, curve (a). The relevant mobility for our experiments will be larger, since the Ge we use has a doping concentration of 2×10^{16} cm^{-3} and its light-hole mass is about half that of GaAs.
[33] T. Klitsner and J. S. Nelson, Phys. Rev. Lett. **67**, 3800 (1991).
[34] A. Pomyalov and Y. Manassen, Surf. Sci. **382**, 275 (1997).
[35] J. E. Northrup and J. Neugebauer, Phys. Rev. B **57**, R4230 (1998).
[36] This 1-D search is performed to an accuracy of $|f_T|/10^6$. We also use this same convergence criterion for our solution to Poisson's equation in the bulk.
[37] J. D. Jackson, *Classical Electrodynamics* (Wiley, New York, 1975), 2nd ed., p. 147.
[38] C. B. Duke, *Tunneling in Solids* (Academic Press, New York, 1969), Eqs. (7.8), (5.10) and (5.17).
[39] E. Merzbacher, *Quantum Mechanics* (Wiley, New York, 1970), p. 194 ff.
[40] L. I. Schiff, *Quantum Mechanics* (McGraw-Hill, New York, 1968), p. 270.
[41] C. B. Duke, *Tunneling in Solids* (Academic Press, New York, 1969), Eq. (6.26).

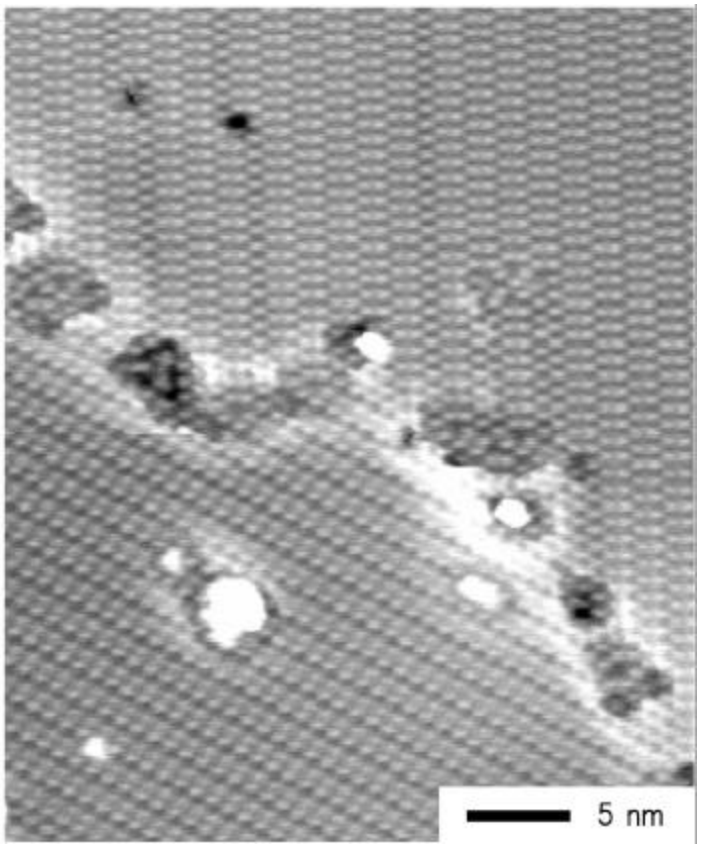

FIG. 1. STM image of the Ge(111)c(2×8) surface, showing a domain boundary separating two domains of the reconstruction. The image was acquired at a temperature of 61 K using a sample-tip voltage of -2.2 V and constant-current of 0.3 nA, and is displayed with a gray-scale range of 0.05 nm.

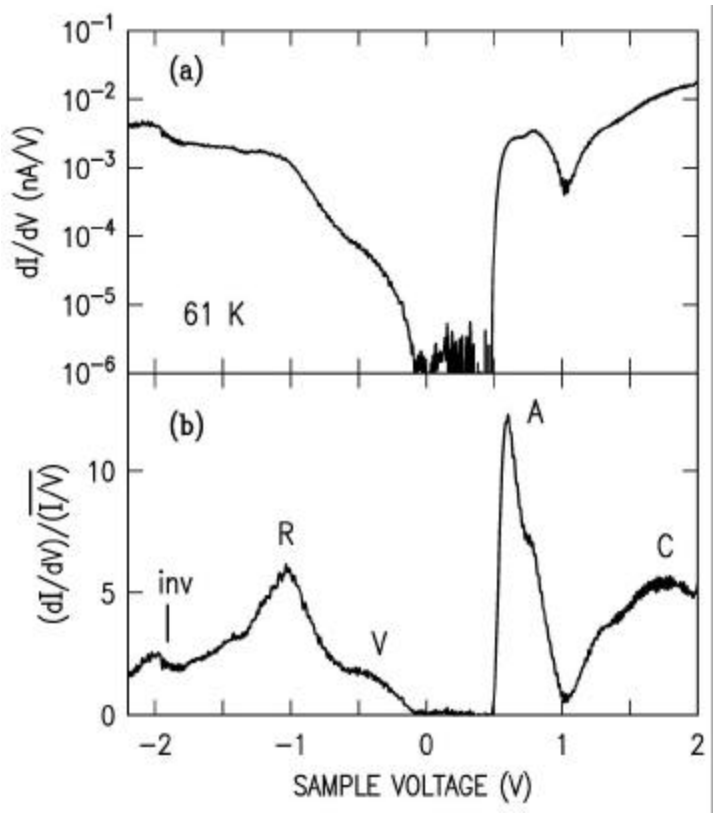

FIG. 2. Tunneling spectrum of the *p*-type Ge(111)c(2×8) surface, displayed as (a) conductance at constant sample-tip separation (on a logarithmic scale) (b) normalized conductance (on a linear scale). The spectrum was acquired at a temperature of 61 K and at a sample-tip separation corresponding to a set-point current of 7 pA at a sample voltage of -2.2 V. Adatom (*A*), rest-atom (*R*), valence band (*V*) and conduction band (*C*) components in the spectra are indicated, as is the voltage below which inversion occurs (*inv*).

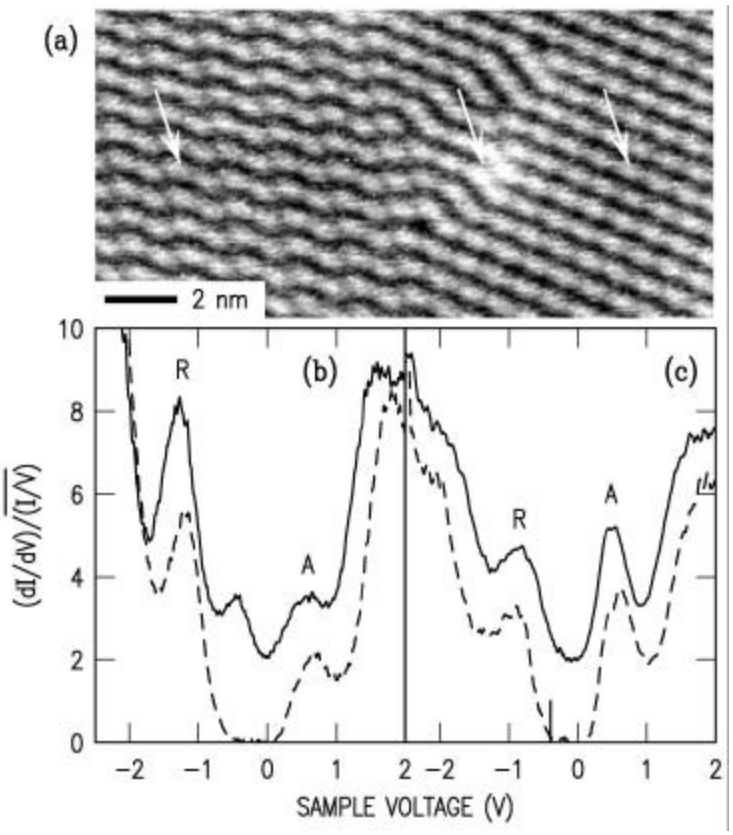

FIG. 3. (a) STM image acquired at room temperature from the *n*-type Ge(111)c(2×8) surface using a sample voltage of + 2.0 V and constant current of 0.1 nA, and displayed with a gray scale of 0.1 nm. (b) and (c) Spectra acquired at ordered (dashed lines) and disordered (solid lines) locations on the surface, with the latter offset by 2 units of the normalized conductance for clarity. Adatom (A) and rest-atom (R) derived states are indicated. The spectra in (b) were acquired from the surface displayed in (a), with the disordered spectrum obtained from the location indicated by the center arrow and the ordered spectrum being an average of those obtained from the locations indicated by the right and left-side arrows.

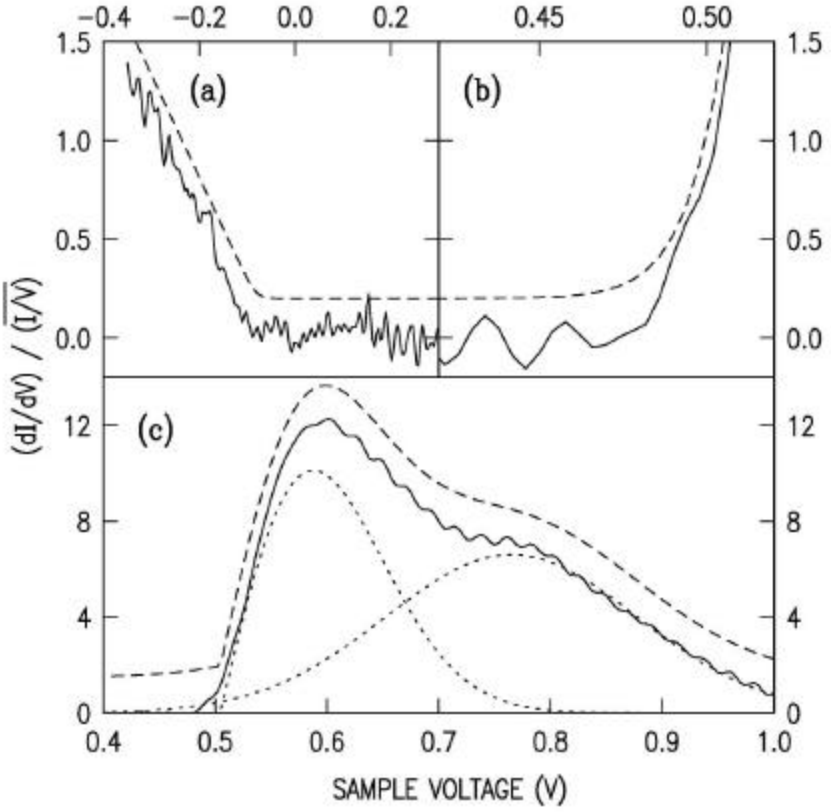

FIG. 4. Fits of the spectral features for the spectrum of Fig. 2: (a) valence band onset, (b) adatom band onset, and (c) entire adatom band. Solid lines show the data and dashed lines (displaced above the solid lines for clarity) show the fits. In (c) the dotted lines show the separate components of the fit function used.

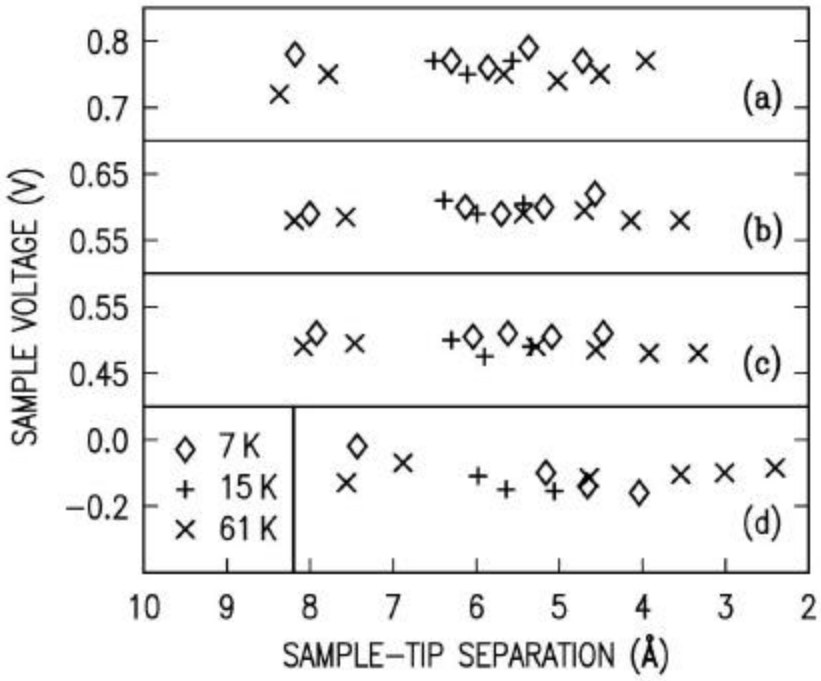

FIG. 5. Observed positions of the (a) upper adatom peak, (b) lower adatom peak, (c) onset of adatom band, and (d) onset of valence band, as a function of the sample-tip separation for each measurement.

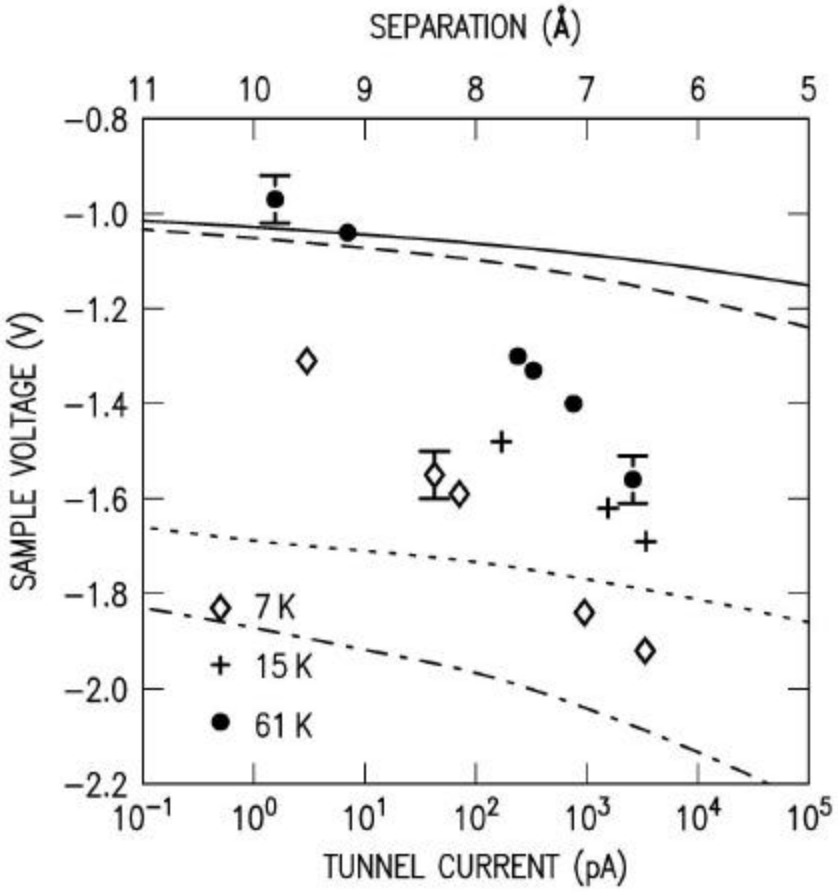

FIG. 6. Observed positions of the rest-atom peak, as a function of tunnel current and for various temperatures. Typical error bars are shown on a few points, indicating the variation in the results at different points on the surface and due to small (unintentional) variations in tip shape. Theoretical curves are shown for equilibrium situations with tip radii of 10 nm (solid line) and 100 nm (dashed line), and for extreme nonequilibrium situations with radii 10 nm (dotted line) and 100 nm (dot-dashed line).

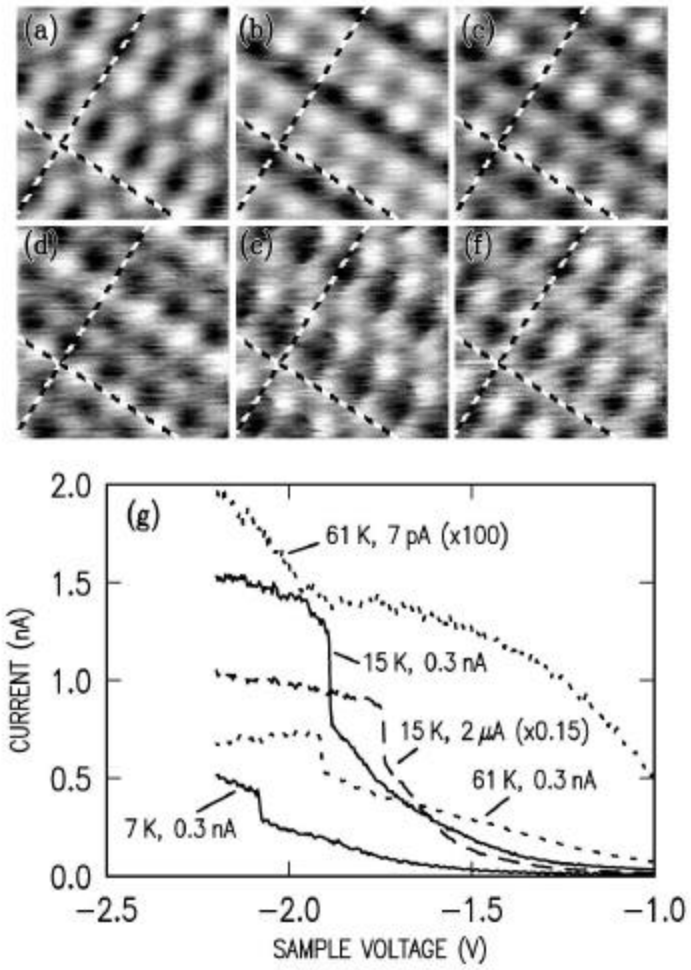

FIG. 7. (a) – (f) STM images of the Ge(111)c(2×8) surface, acquired at sample voltages of $+1.7$, -1.8, -1.9, -2.0, -2.1, and -2.2 V, respectively. All images were acquired at a temperature of 7 K with a constant current of 0.3 nA, extend over 3.6×3.6 nm^2, and are displayed with gray-scales in the range 0.02 - 0.04 nm. (g) Portions of tunneling spectra, acquired at the temperatures and current setpoints indicated.

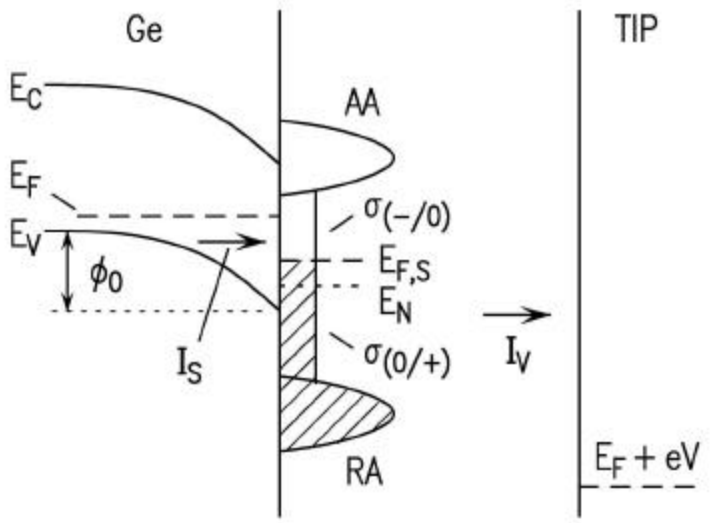

FIG. 8. Schematic energy level diagram for the Ge(111)c(2×8) surface states. Intrinsic surface state bands associated with adatom (AA) and rest-atoms states (RA) are indicated. Bands of disorder-induced states are denoted by s , with the charge neutrality level E_N separating states with different charge character. The electrostatic potential energy at the surface, relative to a point far inside the semiconductor, is denoted by f_0. The surface Fermi-level is indicated by $E_{F,S}$ and the bulk Fermi-level by E_F ; these values are equal for equilibrium between surface and bulk but are unequal for a nonequilibrium situation as shown. An important transport process in establishing equilibrium is the interband current through the semiconductor band gap, I_S. The sample Fermi-level is located at an energy $-eV$ above the tip Fermi-level, with $V<0$ in this diagram.

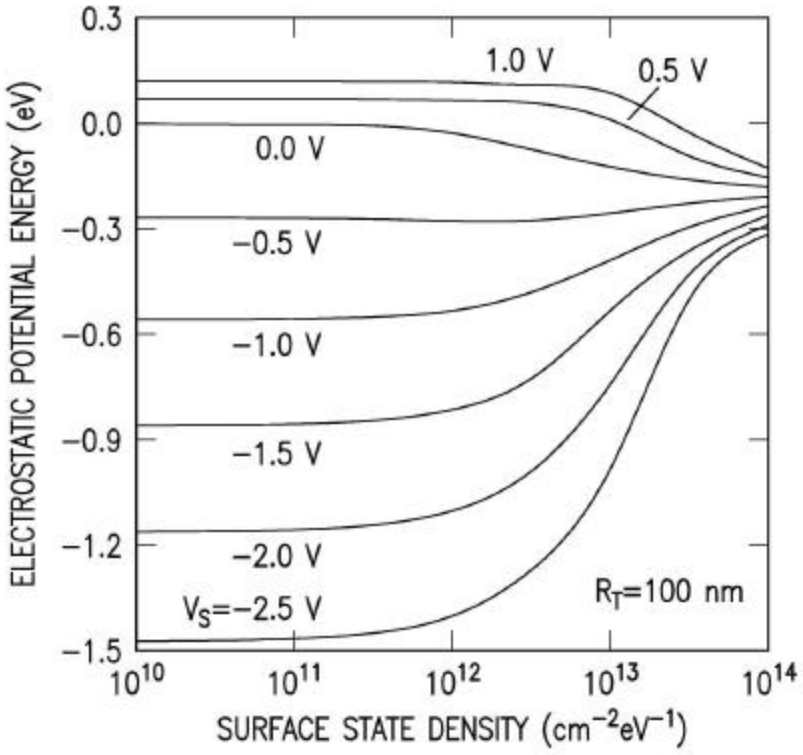

FIG. 9. Computed results for surface potential at a point along the central axis, for *p*-type Ge with doping concentration of 2×10^{16} cm^{-3} and using a 100-nm-radius tip with 0.8 nm sample-tip separation. Results are plotted a function of the density of extrinsic midgap states, with these states being distributed uniformly across the semiconductor band gap and with charge neutrality level of 0.2 eV above the VB maximum. Curves for various values of the sample-tip voltage (assuming zero contact potential) are shown.

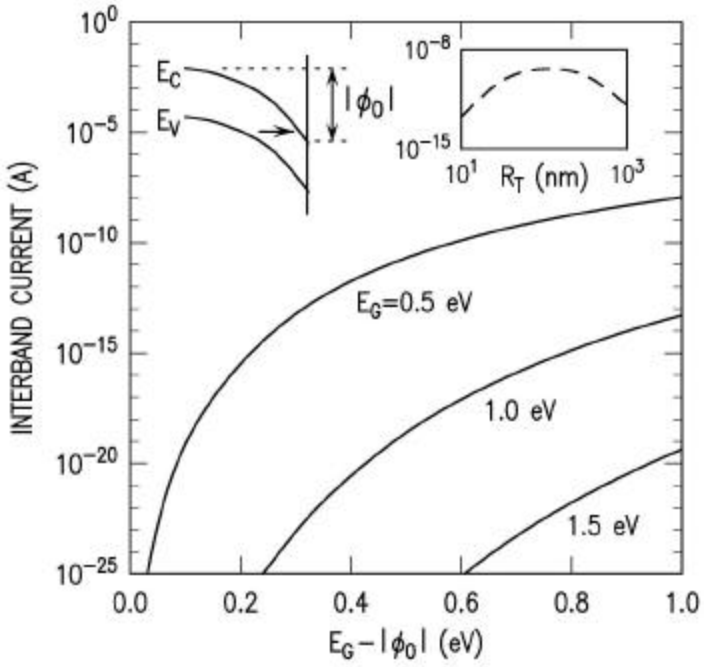

FIG. 10. Computed results for interband current flowing between VB and CB of semiconductors having band gaps E_G as listed, with *p*-type doping concentration of 2×10^{16} cm^{-3} and using a two-band model with effective mass of $0.043m_0$. The solid lines show results for a tip radius of 100 nm, plotted as a function of the energy difference $E_G - \left|f_0\right|$ between the VB maximum far inside the semiconductor and the CB minimum at the surface (the sample-tip voltage is an implicit parameter varied along each line, and a sample-tip separation of 0.8 nm is used). The inset shows the interband current for a 0.5 eV band gap and a sample voltage (assuming zero contact potential) of -2 V, as a function of tip radius.

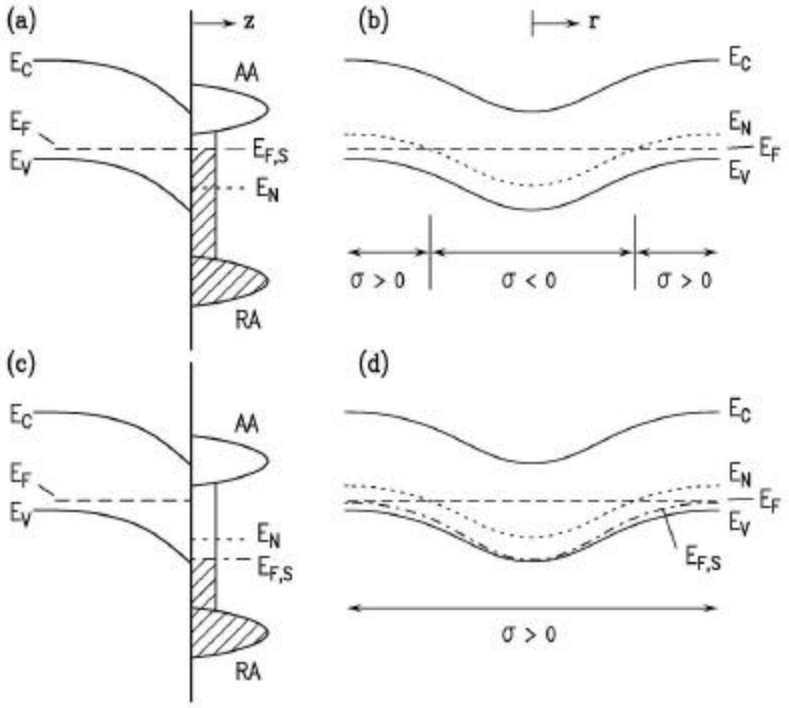

FIG. 11. Schematic energy diagrams of models for occupation of disorder-induced midgap states: (a) and (b) equilibrium, with $E_F = E_{F,S}$; (c) and (d) nonequilibrium, with $E_F \neq E_{F,S}$. Panels (a) and (c) show axial views as a function of *z*, with (b) and (d) showing radial views on the surface as a function of *r*. The sign of the surface state density s at various values of *r* are indicated.

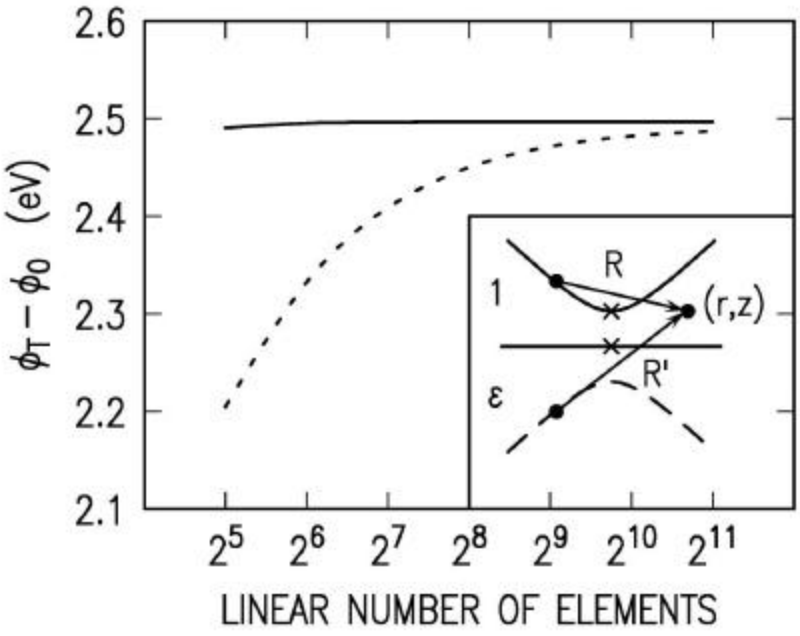

FIG. 12. Convergence of electrostatic solutions, showing the difference between the potential energy at the tip apex (upper x-mark in inset) and on the surface location directly opposite the tip apex (lower x-mark in inset) as a function of the linear number of grid points. Solid line: results from the original problem, with $f_T = 3\,\mathrm{eV}$ being the boundary condition and f_0 being obtained from a finite-element computation. Dashed line: results of the inverse problem, in which the surface charge density on the probe-tip is integrated using the method of images to obtain both f_T and f_0.

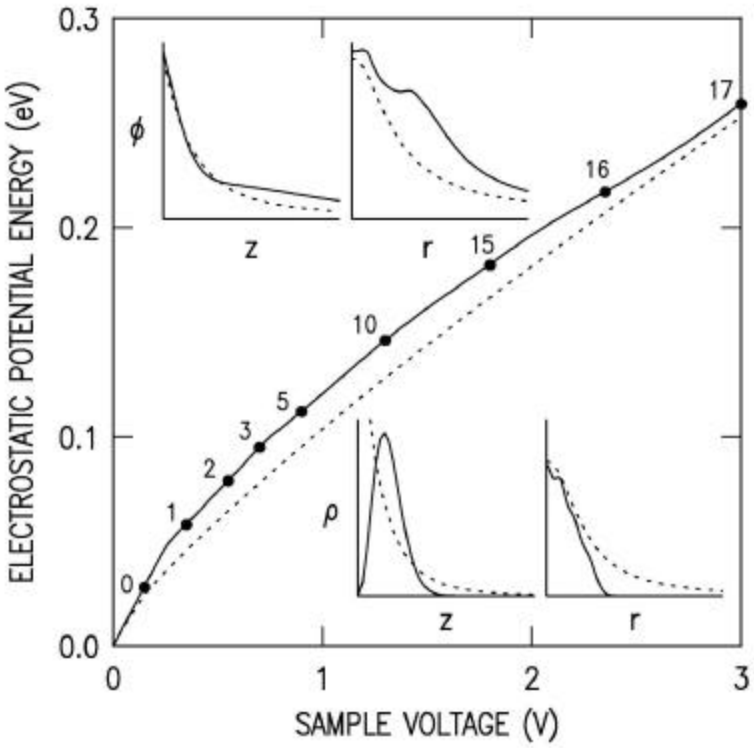

FIG. 13. Computed results for surface potential at a point along the central axis, for *p*-type Ge with doping concentration of 2×10^{16} cm^{-3} under accumulation conditions and using a 100-nm-radius tip with 1 nm sample-tip separation. Results are shown for quantum (solid lines) and semi-classical (dotted lines) computations. The integers along the solid curve indicate the number of quantum states occupied at each point. The insets show two cuts of the potential energy f and the charge density r in the semiconductor for a sample voltage of 2 V: left-side – along the central axis as a function of *z*, and right-side – 1 nm into the semiconductor as a function of *r*. The full-scale range in the insets for f, r, *z*, and *r*, respectively, are 0.2 eV, 0.5×10^{20} cm^{-3}, 10 nm, and 70 nm.

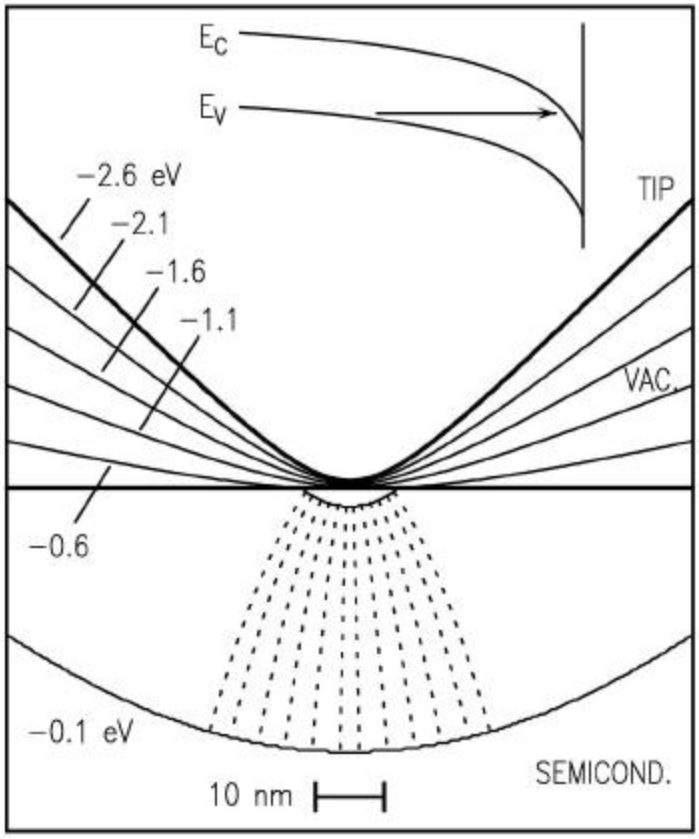

FIG. 14. Equipotential lines (marked in terms of electrostatic potential energy) for a 10 nm radius probe-tip located 1 nm from the semiconductor surface, with the tip biased at $+2.6\,\mathrm{V}$ (energy difference of $-2.6\,\mathrm{eV}$) relative to the semiconductor. The semiconductor is assumed to be *p*-type with doping concentration of $2\times10^{16}\ \mathrm{cm}^{-3}$. The dotted lines show the electric-field lines extending between the -0.1 and $-0.6\,\mathrm{eV}$ equipotentials. These lines correspond to the line-integral paths for evaluating the interband current, for the case of the semiconductor with 0.5 eV band gap and with an electron energy of 0.1 eV below the VB maximum of the semiconductor as pictured in the inset.